Volume 1 | Number 1 | Jan 2013 | Pages 1–100

PCCP

Physical Chemistry Chemical Physics
www.rsc.org/pccp

ROYAL SOCIETY OF CHEMISTRY

Laser-driven phase transitions in aqueous colloidal gold nanoparticles under high pressure: Picosecond pump-probe study

Shuichi Hashimoto,[†]* Tetsuro Katayama,[‡] Kenji Setoura,[‡] Michael Strasser,[†] Takayuki Uwada,[¶] and Hiroshi Miyasaka[‡,]*

[†] Department of Optical Science and Technology, University of Tokushima, 2-1 Minami-Josanjima, Tokushima 770-8506, Japan,

[‡] Division of Frontier Materials Science, Osaka University, 1-3 Machikaneyama, Toyonaka, Osaka 560-8531, Japan,

[¶] Department of Chemistry, Josai University, 1-1 Keyakidai, Sakado, Saitama 351-0295, Japan.

*Corresponding author E-mail: hashichem@tokushima-u.ac.jp, miyasaka@chem.es.osaka-u.ac.jp

Electronic supplementary information (ESI) available.

Graphical abstract 4×8 cm
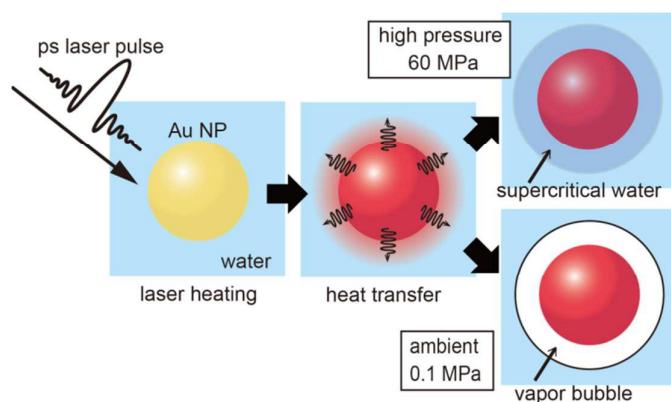
20-word abstract:

Pulsed-laser illumination of aqueous gold colloids under high pressure enables the evaporation from liquid droplets surrounded by supercritical water layer.

Abstract

Pump-probe transient extinction spectroscopy was applied to analyze 355-nm picosecond laser heating-induced phenomena of 60-nm-diameter aqueous gold nanoparticles (AuNPs) under a high pressure of 60 MPa. Kinetic spectroscopy revealed that a supercritical layer surrounding the AuNP nucleated with a lifetime of approximately 1 ns in its dynamic expansion and decay behavior for a fluence of 19.6 mJ cm^{-2}. Moreover, we observed in the post-mortem transmission electron micrographs a number of fragments, a small percentage of size-reduced cores, and erupted particles, among the intact particles after 60 shots, suggesting that evaporation occurs under laser illumination. The particle temperature calculation indicated that evaporation begins with a liquid droplet AuNP surrounded by a supercritical layer at temperatures below the boiling point of gold. By applying high pressure, we are able to obtain a clear picture of the evaporation event, which was not possible at ambient pressure because the forming bubble caused particle temperatures to rise uncontrollably. In this study, we shed light on the critical role of the supercritical layer formed around the AuNP under high pressure during laser-induced evaporation.

Introduction

Gold nanoparticles (AuNPs) exhibit photothermal responses by interacting with visible light; for this reason they have been widely used as nanoheaters,[1,2] photothermal imaging enhancers,[3,4] and vapor bubble generators[5,6] in nanomedicine research and development. The associated physical phenomena have potential in applications such as theranostics of malignant cells in small areas. The underlying principle that provides AuNPs with such intriguing properties is the localized surface plasmon resonance (LSPR) described as the coherent oscillation of conduction electrons when coupled with an electromagnetic field at a particular wavelength of light.[7] The photothermal feature of AuNPs given above plays a critical role, together with the nano-antenna effect that yields practical uses as plasmonic sensors,[8,9] plasmonic photocatalysts,[10,11] and plasmonic solar cells,[12] within the emerging fields of nanoscience and nanotechnology.

To acquire a fundamental understanding of laser−NP interactions that leads to photothermal responses of AuNPs, particular attention has been devoted to the early stages of photo-excitation. Ultrafast spectroscopy studies[13–15] revealed that laser light is first absorbed by the electrons, creating nonthermal electrons. After a few hundred femtoseconds, thermal equilibrium is reached corresponding to the Fermi distribution as a result of electron−electron scattering. Subsequently, the electron energy is transferred to the lattice via electron−phonon coupling (< a few picoseconds), resulting in particle heating. The lattice thermal energy is finally transferred through heat conduction to the surrounding medium through phonon−phonon coupling (< several-tens to several-hundred picoseconds), leading to medium heating at the expense of particle cooling. During cooling, acoustic lattice vibrations [16,17] have been discovered and fully characterized. Moreover, heating-related phenomena, particle melting and evaporation,[18,19] and vapor bubble generation[20,21] immediately surrounding the medium have been observed. Given that these phenomena occur over several tens of picoseconds to a few nanoseconds of excitation, they are difficult to differentiate.

Knowing the time evolution of the particle and medium temperatures initiated by the laser excitation of AuNPs is important because this information is crucial in fully understanding the

heating-induced phase transformations of the particle and the surrounding medium. For this purpose, transient extinction spectroscopy is promising because temperature-induced bleaching has been known to occur for the LSPR band, and the bleaching intensity is correlated with particle temperature.[22] Besides particle temperature, changes in the medium refractive index caused by heat transfer and bubble generation affect the transient spectra. The former accounts for medium temperature-dependent LSPR bleaching because of changes in refractive index whereas the latter is affected in a complicated manner depending on bubble diameter.[22] At ambient pressure, the bubble signals, especially the scattering signals, contribute greatly to the transient extinction spectra and the extinction signals arising directly from the particle were obscured. Introducing high pressures, however, may improve the acquisition of optical signals from the particle because high pressures exceeding the critical pressure, 22.1 MPa [23] for water presumably suppress bubble formation.

Here we describe the transient spectroscopic study of AuNPs by excitation with a 15-ps pulse, when an external pressure of 60 MPa is applied. The transient signals in conjunction with temperature simulations are used to characterize the particle temperature evolution and changes in refractive index of the surrounding medium. The picosecond laser excitation is appropriate for two reasons. First, despite the short pulse duration, nonlinear effects such as multi-photon absorption-induced plasma generation[24] can be avoided and purely photothermal processes are pursued. Second, the excitation is completed before a significant temperature increase occurs for both particle and medium. This is advantageous in tracking the temperature-induced melting and evaporation of AuNPs. If a nanosecond laser pulse is used for excitation, both particles and medium are heated alike during the pulse duration, making the spectroscopic analysis difficult. The application of 60 MPa completely suppresses vapor bubble formation from water; in its place, a supercritical layer was formed. We revealed that liquid AuNPs surrounded by a supercritical water underwent surface evaporation at temperatures between the melting and boiling points of bulk gold. Hence, we could obtain a picture of laser-induced phase transitions of both AuNPs and surrounding water under high pressure.

Experimental

Sample

An aqueous solution of AuNPs with nominal diameters of 60 nm (cat. #: EMGC60) was purchased from BBI Solutions (Cardiff, UK). The particles were synthesized using a variation of the Frens citrate reduction method, and were stabilized with citrate.[25] The particles were transformed to a spherical shape from their original faceted shape by irradiating with weak-intensity 5-ns laser pulses of wavelength 532 nm (~10 mJ cm^{-2}). The particle images were acquired using a transmission electron microscope (TEM) and the corresponding size distribution (59 ± 4 nm) were obtained. The molar concentration of AuNPs is 4.3×10^{-11} M ($A_{534 \, nm} = 1.35$ for an optical path length of 1.0 cm).

Instrumentation

A picosecond pump-probe system with a custom-built mode-locked Nd^{3+}:YAG laser was used to measure the transient spectra.[22] Third-harmonic light (355 nm) with an FWHM of 15 ps as a pump pulse was focused using an f = 200-mm lens into a spot of diameter 2.0 mm. The irradiation with 355-nm wavelength light (power fluctuation < 10%) excited the interband transition of the AuNPs. Note that interband excitation is basically similar to LSPR excitation, resulting in hot-electron generation and eventually particle heating. The picosecond white-light continuum generated by focusing a fundamental pulse into a 10-cm quartz cell containing a 3:1 D_2O and H_2O mixture was used as a probe light that covers a spectral window from 400 to 1000 nm. Circularly polarized probe light was guided into the center of the 2.0-mm spot defining the pump area. Two polychromator Monospec 27 (Jarrell Ash, Grand Junction, CO) − multichannel photodetector S4874 (Hamamatsu Photonics, Hamamatsu, Japan) sets were used to detect the probe light intensity. The transient signals at a given time delay were obtained by calculating $\log_{10}\{I_0(\lambda) / I_p(\lambda)\}$. Here, $I_0(\lambda)$ represents the intensity of the probe light at wavelength λ without excitation, and $I_p(\lambda)$ is the probe light intensity with excitation. In the transmittance-mode experiments on the AuNP colloidal solutions, both absorption and scattering contribute to the steady-state and the transient spectra (extinction = absorption + scattering). Hence, the transient signal obtained using the quantity $\log_{10}\{I_0(\lambda) / I_p(\lambda)\}$

corresponded to a Δextinction. The repetition frequency of the pump laser light was 0.5 Hz. The time resolution of the detection system was about 15 ps. The energy of the picosecond laser light at 355 nm was measured using a ED-200 power meter (Gentec EO, Quebec, Canada). The precision of the measured fluence was ± 0.1 mJ cm^{-2}. To apply a pressure of 60 MPa, a cuvette was placed in a hydrostatically pressurized container that enabled solution agitation.[26] Most of the data were accumulated over the course of four measurements. The errors for the transient extinction values were < ± 10%, as estimated using the standard deviation of the signals before the time origin, and the spectral resolution was approximately 3 nm. The chirping of the probe white light continuum was corrected. All measurements were performed at 22 ± 1°C.

TEM images of the particles were recorded on a JEM-2100F (JEOL Ltd., Tokyo, Japan) microscope operated at 200 kV. Specimens for the TEM measurements were prepared by placing one drop of a sample solution onto a support made of Cu mesh coated with an evaporated 13-nm-thick carbon film. The support was dried in vacuum. The preparation of TEM specimens was performed on the same day as the laser irradiation. Software, Image J (http://rsbweb.nih.gov/ij/), was used for processing particle images.

Temperature and spectral simulations

To calculate the temperature evolution of free electrons and lattice systems after fast pulsed-laser excitation of AuNPs, we used the two-temperature model (TTM) described via coupled heat equations for T_e (electron temperature) and for T_L (lattice temperature).[13–15] Subsequently, the heat flux into the surrounding medium leads to particle cooling. Hence, the model was extended to include the medium in which radial heat conduction is responsible for cooling.[27] Details of the TTM calculation are described in **Electronic Supplementary Information (ESI), S1**. As given in ESI, S1, we used temperature-dependent density, heat capacity, refractive index, thermal conductivity and dielectric constant of water at 60 MPa for the calculation. We can safely assume that the boiling of water may not occur at 60 MPa. To describe thermal expansion of Au, we used experimental temperature-dependent density. We neglected the melting enthalpy of Au in the calculation. In the

6

nanosecond time regime, heat transfer to the surrounding medium creates a local temperature gradient in water adjacent to the AuNP. Under such circumstances, the refractive index of water as well as the temperature gradient changes with time. Thus, a multi-core-shell extension of the Mie theory was applied to calculate the absorption cross-section, C_{abs}.[28–30] In the model, an AuNP of homogenous temperature is surrounded by a number of water layers, each of which is characterized by a shell thickness and constant refractive index. Furthermore, the dielectric function of gold is described by the sum of the intraband contribution (Drude term) and the *5d* to *6sp* interband transition.[15,31] In this work, we used Otter's experimental temperature-dependent complex refractive indices to obtain the temperature-dependent LSPR spectra at temperatures: ambient temperature, 583 K, 843 K, 1193 K, and 1336 K (liquid).[32]

Results and Discussion

1. Excitation-induced dynamics in aqueous colloidal AuNPs at 60 MP.

Figure 1 shows transient extinction spectral changes observed at two fluences, 4.5 mJ cm^{-2} and 19.6 mJ cm^{-2}. For excitations at 4.5 mJ cm^{-2}, a negative extinction signal around 525 nm and positive extinctions at 440−500 nm and 550−650 nm emerged almost within the response time of the detection system, reaching a maximum at 20−40 ps and then decaying with time. The decay consisted of two stages: a fast decay within 100 ps was followed by a slow decay that persisted up to 6 ns. Both the positive and negative extinctions return to almost zero extinction after a time delay of 6 ns. Thus, the transient spectral changes clearly show the time-dependent LSPR band bleaching followed by recovery. This can be ascribed to the laser-induced particle heating, which corresponds to the LSPR band broadening (**ESI, S2**) and subsequent particle cooling induced by heat transfer to the medium, leading to the LSPR retrieval.[13–16,33,34] The spectral changes consisting of strong negative extinctions around the plasmon peak position accompanied by small positive extinctions at both wings of the plasmon band occurred with isosbestic points at ~490 nm and ~560 nm when laser fluences were low (Fig. 1a) and more clearly at fluences of 1−2 mJ cm^{-2} and for which the

medium temperature increase is insignificant. However, when the medium heating is significant at a high fluence such as 19.6 mJ cm^{-2}, the isosbestic points were lost (Fig. 1b) because of gradual medium heating-induced refractive index reduction that leads to appreciable minus Δextinctions at time delays of 50–100 ps.

To see more clearly the time- and fluence-dependent events, we looked into the time profiles at a few wavelengths representing typical kinetics at 60 MPa (**Fig. 2**). Consistent with a larger fluence, a greater extent of bleaching and a slower extinction recovery were observed at 19.6 mJ cm^{-2} than at 4.5 mJ cm^{-2}. The time profile at 490 nm is worth noting. As an inflection point occurs for the temperature-induced bleaching of LSPR band at this wavelength, the extinctions are nearly zero before initial 40 ps (Fig. 2b). However, the extinction at 490 nm decreased up to 100 ps, more pronouncedly at high fluences. This suggests that medium heating takes place during this period with notable delay with respect to the laser pulse, suggesting the real-time observation of heat transfer at NP-water interface at this time scale.

At a fluence of 19.6 mJ cm^{-2}, the bleaching signal at the LSPR peak position persisted over the optical delay range of our pump-probe measurement (Fig. 2c). This suggests that particle and medium cooling takes a longer time at high fluences. We measured the transient extinction signal at 532 nm as a function of time, using a continuous-wave laser as a probe light and a photodiode (rise time < 1 ns) as a detector (**ESI, S3**). Bleaching remained constant, without recovering to the baseline, for delays from 100 to 500 ns. This can be indicative of permanent bleaching of the LSPR band. The observation is consistent with the slight reduction in the peak intensity of extinction spectrum after irradiation at 19.6 mJ cm^{-2} for 60 shots, suggesting that the particle size reduction occurred for a portion of particles exposed to the laser beams as will be described in Section 3.

Peculiar kinetics that occurred at 19.6 mJ cm^{-2} caught our attention. The LSPR bleaching time profile exhibited a zig-zag appearance within the initial 1 ns before decaying. For example, at wavelengths of 470 nm (Fig. 2a) and 600 nm (Fig. 2d), within 40 ps the positive extinction reached maximum. However, instead of the monotonic decay to the baseline that was observed for 4.5 mJ

cm^{-2}, negative extinction was obtained reaching a plateau at 100–200 ps, then increased again up until 500 ps and decreased later, finally converging to extinction zero. An analogous zig-zag behavior was also observed at 525 nm (Fig. 2c), corresponded approximately to the LSPR peak wavelength. At this wavelength, the initial strong minus extinction occurred until 200 ps, then bleaching recovered up to 500 ps. Afterwards, the minus extinction increased but turned again and decreased after 1 ns. The explanation for the observed zig-zag time profiles must wait until the discussion based on temperature profiles of the supercritical layer around AuNPs.

The effect of high pressure on the transient extinction spectra observed here deserves attention, *i.e.*, the suppression of a vapor bubble from water around the NP results in big spectral changes. **Figure 3a and b** compares the fluence-dependent transient spectra at atmospheric pressure of 0.1 MPa with those at 60 MPa (time delay: 2 ns for a and 400 ps for b). At 0.1 MPa, because of intense Rayleigh scattering from a bubble formed around the NP, the spectral envelopes above the bubble generation threshold (4.5–5 mJ cm^{-2}) are more severely floated from the baseline (extinction zero line) as fluence increases. This was clearly observed at wavelengths at both ends of the spectra. Despite the interference from the scattering, dips centered at around 520–530 nm are still visible, which is indicative of LSPR bleaching resulting from particle heating. In contrast, the spectral floating from the baseline was absent at 60 MPa even at high fluences equivalent to that causing severe bubble formation at ambient pressure, suggesting bubble formation was suppressed at such a high pressure.
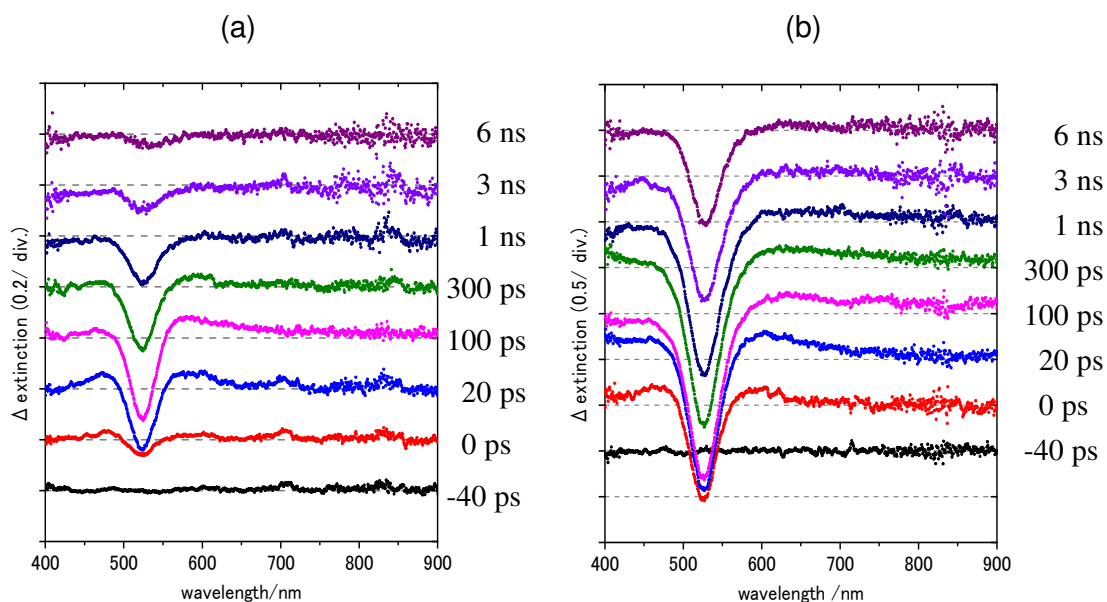

(a)   (b)

Fig. 1 Transient extinction spectra of aqueous colloidal AuNPs with a 60-nm-diameter at the fluence of 4.5 mJ cm^{-2}, (a) and 19.6 mJ cm^{-2} (b) at various delays from the bottom to the top from −40 ps to 6 ns. The excitation was provided by a 15-ps (FWHM) laser pulse at a wavelength of 355 nm for an AuNP solution. Time delays are given on the right of each graph. The spectra were shifted with time delays from lower to upper by the extinction value of 0.2 in (a) and 0.5 in (b).
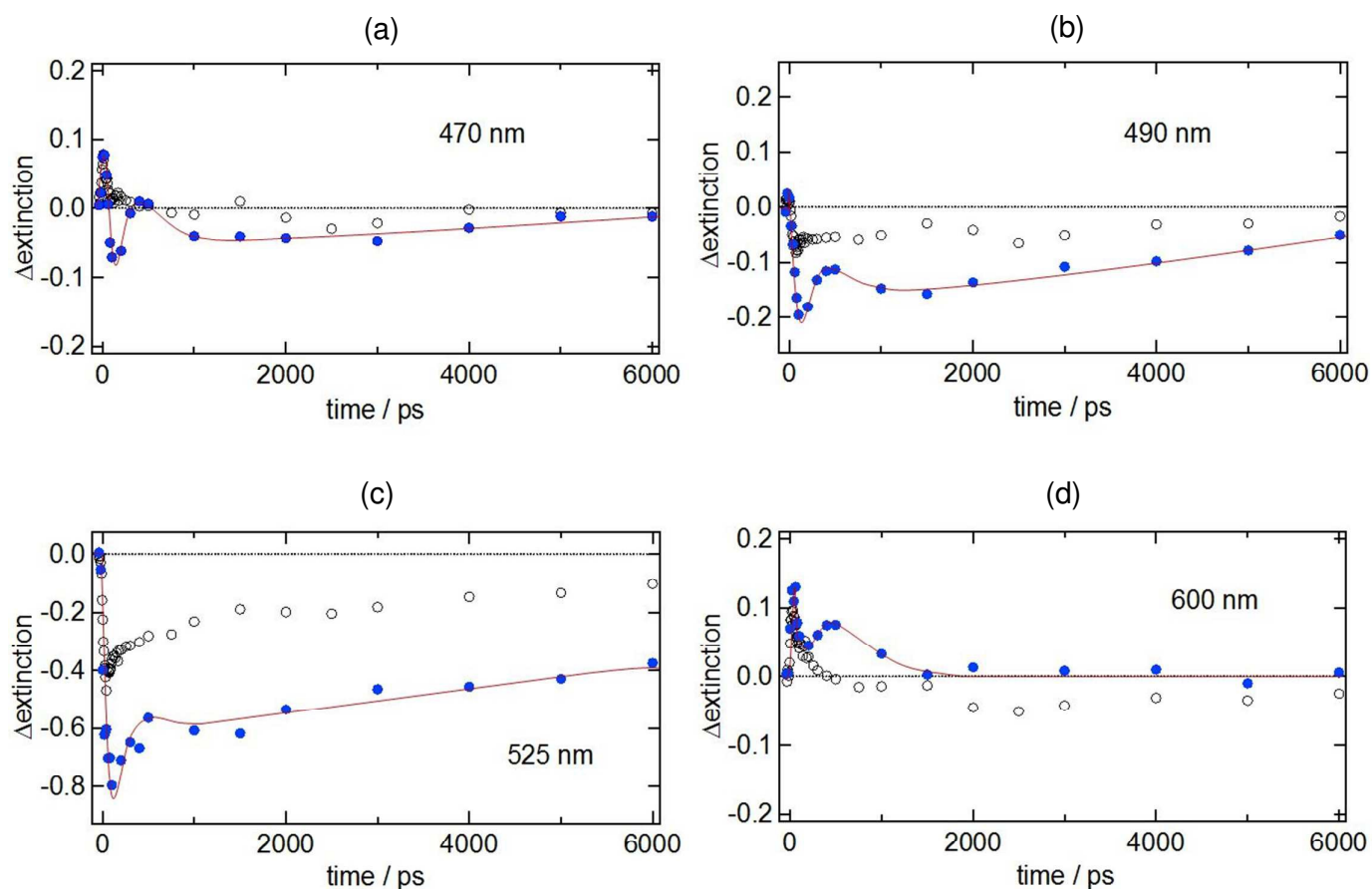

Fig. 2 Time evolution of transient extinction at a fluence of 4.5 mJ cm^{-2} (open circles) and 19.6 mJ cm^{-2} (blue closed circles) for 60-nm-diameter AuNPs. Monitoring wavelengths: (a) 470 nm for the left-hand wing, (b) 490 nm for approximately the isosbestic point of LSPR bleaching at low laser fluences, (c) 525 nm for the LSPR peak position, and (d) 600 nm for the right-hand wing in LSPR-band bleaching. Solid red lines are drawn as visual guide.
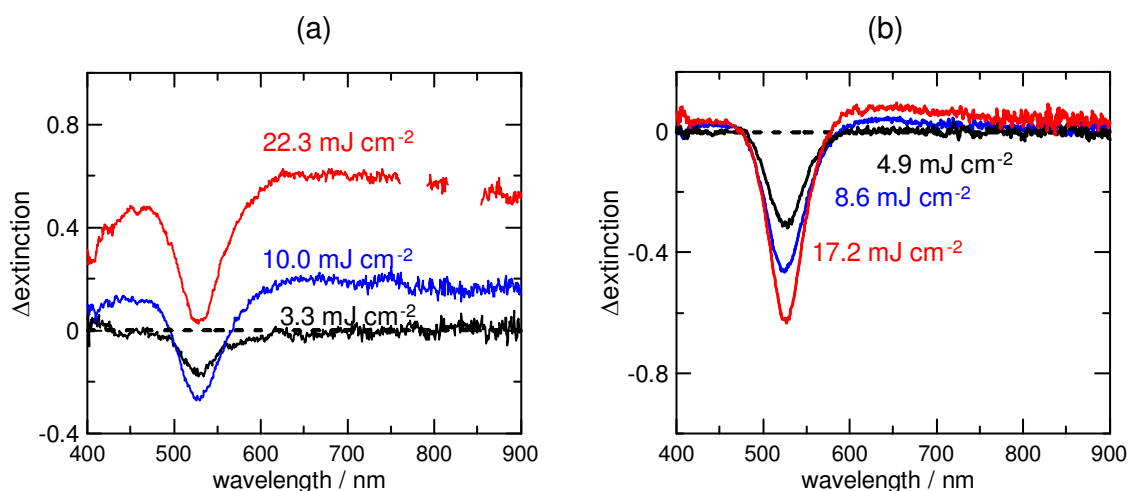

(a) (b)

Fig. 3 Fluence-dependent transient extinction spectra of aqueous colloidal AuNPs of 60-nm diameter: (a) for atmospheric pressure (0.1 MPa) [22] and (b) under a pressure of 60 MPa. The numbers in the figure represent fluences applied. Time delay: 2 ns for (a) and 400 ps for (b). The threshold fluence of bubble formation at 0.1 MPa is 4.5–5.0 mJ cm^{-2}.

----

2. Interpretation of transient spectra based on NP/medium temperature simulation.

The major outcome of the laser–AuNP interaction in our picosecond laser experiment is heat generation under the experimental excitation with peak power densities of $< 10^9$ W cm^{-2} (≤ 20 mJ cm^{-2} for a 15-ps pulse) that preclude multiphoton excitation. Remember that these multiphoton processes can occur at fluences $\geq 10^{15}$ W cm^{-2}.[35,36] **Figure 4** shows the time profiles of various temperatures: electron temperature (T_e), lattice temperature (T_L), and medium (water) temperature (T_m) at the AuNP surface, calculated using TTM [13–15, 27] for excitations with three fluences, 5, 10, and 20 mJ cm^{-2}, approximately the experimental laser intensities. Notably, the temperature gap at the NP-water interface was shown to arise from the interfacial thermal conductance G. The effect of G values on the calculated temporal temperature profile is shown in **ESI S4**. According to ESI S4, the temporal behavior of T_L was not affected by different G values but the temporal profile of T_m at the particle interface was appreciably affected. In our calculation, we used a temperature-dependent G given by $G = 3C_m k_m / r C_L$ in which C_m is the heat capacity of the medium water, k_m is the

12

thermal conductivity of water, r is the particle radius, and C_L is the heat capacity of particle.[37] The

equation gives $G = 100$ MW m^{-2} K^{-1} for the 60-nm-diameter particle at room temperature.

Experimentally, a value of 100 MW m^{-2} K^{-1} was measured at temperatures near room temperature

for citrate-capped AuNPs (35-nm diameter and 18-nm diameter) previously.[38,39] We do not provide

a detailed discussion of an appropriate G value because there is little information regarding a solid

theoretical background to estimate proper G values at high temperatures of $T_L \geq 1000$ K, and such

work, therefore, goes beyond the scope of this study.

According to the TTM result given in Fig. 4, T_e equilibrates with T_L within 50 ps and the

maximum T_e reached is ≤ 5000 K (for ≤ 20 mJ cm^{-2}). This implies that a non-photothermal process

because of a high T_e is negligible in our case.[40] Instead, the time evolutions of T_L and T_m are

relevant to interpret the observed transient spectra except in the initial 50 ps where the decay of T_e

is responsible. The fluence-dependent values of T_L immediately after the excitation are 750 K for 5

mJ cm^{-2}, 1200 K for 10 mJ cm^{-2}, and 2000 K for 20 mJ cm^{-2}; T_L decayed with time because of heat

transfer to the surroundings. Previously, a TTM-based estimation of a threshold T_L for the vapor

bubble formation in aqueous colloidal AuNP (d = 60 nm) under atmospheric pressure gave a T_L

value of 1200 K that is adequate from the observation of particle melting on picosecond laser

excitation with a fluence of 4.5–5.0 mJ cm^{-2} to nucleate bubble.[22]

As seen in Fig. 2, the initial fast decay is followed by a slow decay to the Δextinction zero for

LSPR at 4.5 mJ cm^{-2}, for typical wavelengths of 470 and 600 nm. This also occurs for the bleaching

recovery of the LSPR peak at 525 nm. The observed time-dependent decay/recovery profiles are

consistent with the time profile of T_L in Fig. 4a; and this suggests that particle cooling is responsible

for the transient LSPR decay. For 19.6 mJ cm^{-2}, T_m at the particle surface (Fig. 4c) increases with

time from 1000 K at 100 ps to 1300 K at 6 ns. T_m is also a function of distance from the

particle-water interface as well as a function of time. Thus, the spatio-temporal T_m and medium

refractive index profiles calculated by the TTM were given in **Fig. 5**. From Fig. 5, the condition for

the supercritical water formation is not met at 5 mJ cm^{-2} (Fig. 5, upper left panel) because the

supercritical state of water forms at $T_m > 647$ K and p > 22.1 MPa.[23] At 10 mJ cm^{-2}, the calculation suggests that the supercritical layer forms but only at the close vicinity of particle surface (Fig. 5, middle left panel). Meanwhile, the fluence of 19.6 mJ cm^{-2} can give conditions well exceeding the supercritical water formation at the surrounding water layer of the particle surface (purple line in Fig. 5, lower left panel).

To interpret the experimental transient spectra, the spectral simulation was performed using Mie theory. We assumed that a 60-nm-diameter AuNP core, surrounded by 10-shell water layers with increasing refractive indices from inside to outside, was submerged in water at an ambient temperature (refractive index of 1.348 at 60 MPa).[41,42] For the spectral simulation, both the particle temperature and the medium temperature profile at a given time delay were considered. Note, however, that only T_L with experimentally available complex refractive indices (room temperature, 583 K, 843 K, 1193 K, and 1336 K (liquid)) were used. To obtain the transient spectra, we first calculated the extinction cross-sectional (C_{ext}) spectra of a single AuNP at room temperature, C_{ext} (*RT*) and at temperature T_L, C_{ext} (T_L). Then, the difference, $\Delta C_{ext} = C_{ext}$ (T_L) $-$ C_{ext} (*RT*) was calculated for various wavelengths, yielding the transient spectrum. The ΔC_{ext} *vs.* wavelength spectra thus obtained compares well with the experimental extinction *vs.* wavelength spectra under the assumption that extinction is expressed as a function of C_{ext} [m^2], particle concentration N [m^{-3}], and optical path length d [m], given using $extinction = 0.434\, C_{ext}\, N\, d$.

Figure 6 shows the simulated ΔC_{ext} *vs.* wavelength spectra that were in reasonable agreement with the experimental extinction spectra, although an attempt was not made to construct precise time curves because of limited numbers of T_L with known refractive indices available for the Mie calculation. At a low fluence of 4.5 mJ cm^{-2}, we basically observed the LSPR bleaching recovery represented by the disappearance of positive wings and the recovery of negative extinction with time. This was well reproduced in the simulated ΔC_{ext} spectra for 5 mJ cm^{-2} given in Fig. 6a. The spectral change was mainly caused by a time-dependent decrease in T_L because the medium temperature increase was not so strong. For a high fluence of 19.6 mJ·cm^{-2}, three types of spectra

were observed during the decay: the initial LSPR bleaching with two positive wings (type I) quickly

decayed to form asymmetric shape with the left wing being shifted downward to negative values

whereas the right wing remaining positive (type II), followed by downward spectral shift of the

right wing of the LSPR (type III). At the high fluence, an AuNP was assumed to be transformed to a

liquid droplet with $T_L \geq 1336$ K from the temperature simulation. In spectral simulations, three

typical spectral shapes were reproduced (Fig. 6b) depending on the medium temperature profile.

The simulation showed that the left side of the LSPR band is more strongly affected by medium

refractive index reduction. The asymmetric bleaching spectral shape (Fig. 6b, blue line

corresponding to type II) occurs at the initial stage of excitation, when the medium temperature

profile is very steep near the particle surface with a low refractive index of ~1.1 because heat

transfer from the medium is still incomplete. Later, a downward spectral shift of the right wing of

the LSPR band results (Fig. 6b, red line). Here, because heat continues to conduct into the medium

with time, the region of decreased refractive index expands. Accordingly, the medium temperature

profiles greatly affect the transient spectral shapes at high fluences.

We now return to the issue of the small zig-zag signal superimposed on the Δextinction vs.

time curve observed at the initial 0.1 ns–1.0 ns of LSPR decays at a high fluence of 19.6 mJ cm^{-2}

(Fig. 2). The observed zig-zag signal is reminiscent of bubble dynamics, *i.e.*, nucleation, expansion,

and collapse that were observed previously by applying the transient extinction spectroscopy.[22] For

a bubble, the Δextinction initially decreases because bubble nucleation causes the refractive index

reduction in the medium immediately surrounding AuNP. The Δextinction next increases as the

bubble expands because of increased scattering from the bubble surface. Finally it decreased

because of collapse. The big difference at high pressure is a much smaller signal intensity than that

for the bubble and the time scale of observation. A much longer lifetime for the bubble of 10 ns is

observed for a 60-nm AuNP excited by 5 mJ cm^{-2} of a 15-ps pulse at 355 nm. In analogy with a

vapor bubble, the zig-zag signal at high pressure can be ascribed to the dynamics of supercritical

layer nucleation, expansion, and collapse. At first, we assumed that the calculation of T_L and T_m can

fully explain the transient kinetics. However, the medium temperature profiles (Fig. 5) are a static picture that ignores the phase transition. In other words, the supercritical layer formation is an abrupt event distinct from the liquid state and cannot be treated as a continuum model.

At this moment, a rigorous simulation of the supercritical layer dynamics is not feasible, therefore, we tentatively used a bubble-like model, *i.e.*, a spherical AuNP surrounded by a concentric spherical supercritical layer of refractive index 1.1 submerged in water of refractive index 1.348 at 60 MPa. Using Mie theory, we calculated the extinction spectra for various supercritical layer thicknesses. The result (see **ESI, S5**) shows that the bubble model can qualitatively explain the zig-zag Δextinction time behavior in terms of supercritical layer expansion and collapse. For instance, referring to Fig. 2a, we see that the Δextinction at the wavelength of 470 nm increases from a negative value to zero at time delay of 500 ps. Moreover, the ΔC_{ext} vs. diameter curve for wavelength of 470 nm **(ESI, S5)** shows that a supercritical layer thickness of ~80 nm can be reached for $\Delta C_{ext} = 0$. This 80-nm thickness is a rough estimation of the maximum supercritical layer from optical extinction measurements. Indeed, the reason for the short lifetime is the high pressure that acts to crush the layer formed by the phase transition.

Contrary to expectation from the static picture, our transient spectroscopic measurement reveals that supercritical layer around AuNP formed under high pressure exhibited a dynamic nature of growth and collapse, similar to a vapor bubble that nucleates at ambient pressure. The physical properties of the supercritical layer compared with those of the vapor bubble deserve comment. Table 1 shows the basic properties for both vapor bubble and supercritical water.[43] One important attribute of a supercritical layer is the near order-of-magnitude larger thermal conductivity than that of a vapor bubble. Therefore, heat transfer in a supercritical layer is as efficient as in liquid water although it is inhibited in a vapor bubble. Optical properties of a supercritical layer such as light scattering are similar to those of a vapor bubble because of similar refractive index values; therefore, except for intensity, it is difficult to differentiate the two species spectroscopically. The big difference in the two is density (Table 1). Although we could avoid vapor bubble generation by

16

applying a pressure exceeding the critical pressure of solvent, the dynamic occurrence and dissipation of the supercritical layer may interfere with the optical measurement of AuNPs at the early excitation stage of several tens of picoseconds to nanoseconds.
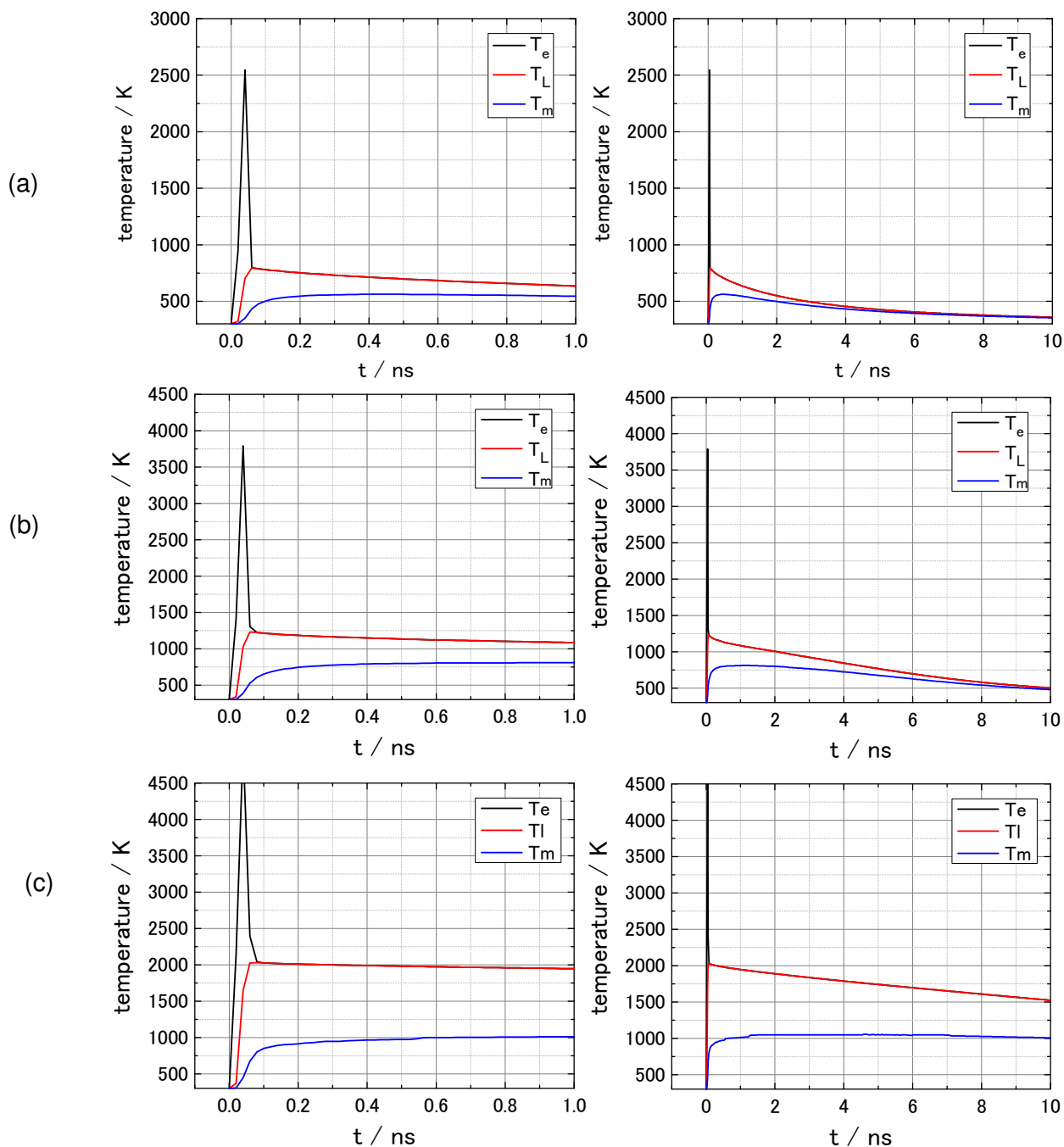
Fig. 4 Simulated temporal evolution of the electron temperature T_e (black line), the lattice temperature T_L (red line), and the maximum water temperature T_m at the NP−water interface (blue line) for a 60-nm-diameter gold sphere absorbing a 15-ps laser pulse (the FWHM of the Gaussian time profile) at 355 nm and at laser energy densities of 5 mJ cm^{-2}, where $P_{max}= 1.5 \times 10^8$ W cm^{-2} (a), and 10 mJ cm^{-2}, where $P_{max}= 3.0 \times 10^8$ W cm^{-2} (b), and 20 mJ cm^{-2}, where $P_{max}= 6.0 \times 10^8$ W cm^{-2} (c). Calculation showing that T_e equilibriates with T_L within 50 ps.

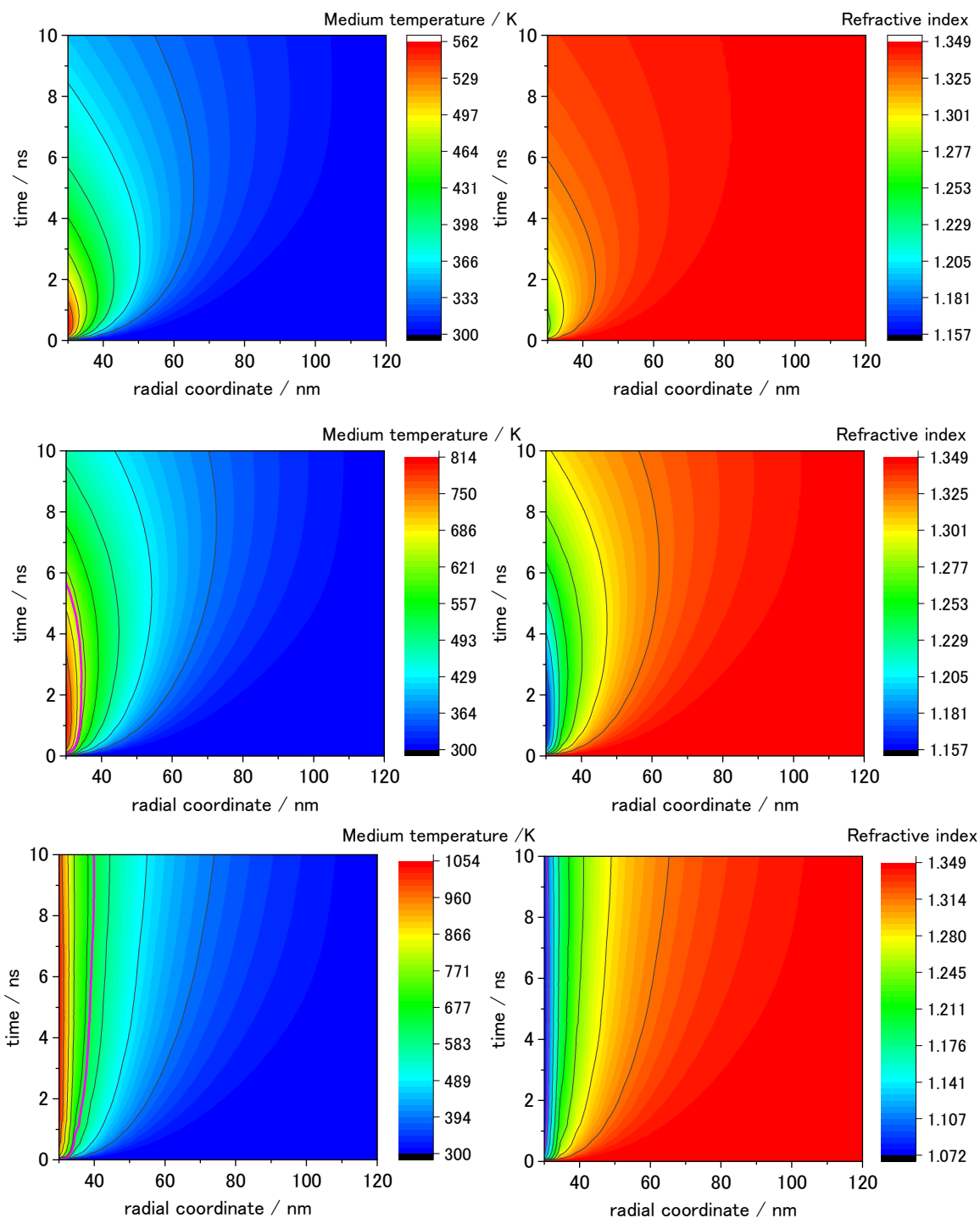---

18

Fig. 5 Simulated spatio-temporal evolution of water temperature (left) and refractive index (right) at various laser fluences: upper panel, 5 mJ cm^{-2}; middle panel, 10 mJ cm^{-2}; lower panel, 20 mJ cm^{-2}.
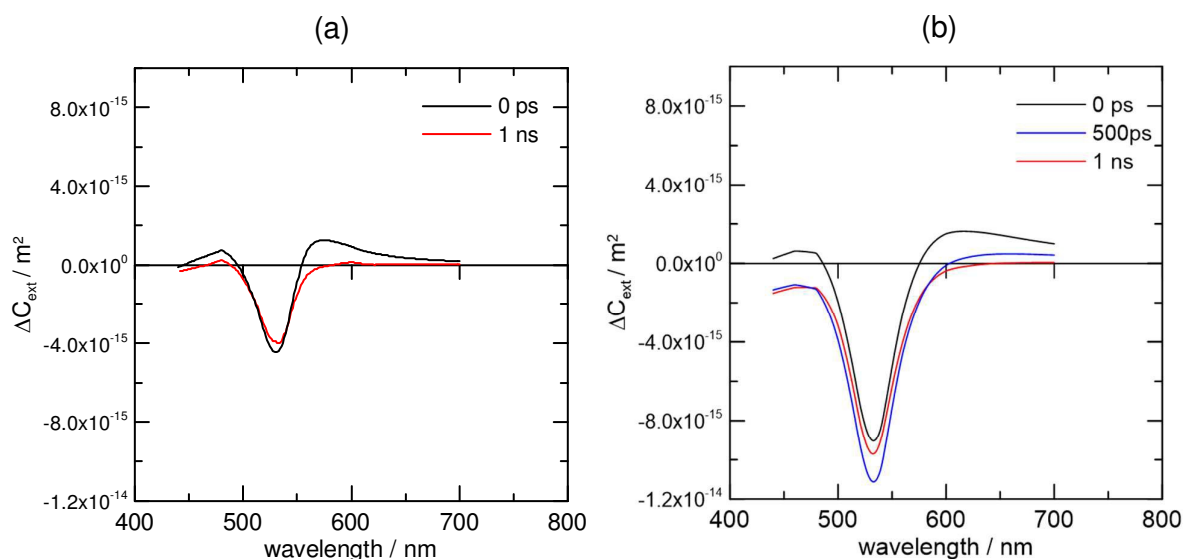
19

Fig. 6. Simulated transient extinction cross-sectional (ΔC_{ext}) spectra with time delays for a AuNP surrounded by 10 spherical water shells (each thickness: 4.5 nm) of various refractive indices with increasing order from inside to outside, submerged in water (refractive index: 1.348 at 60 MPa). Applied laser fluences for the simulation: 5 mJ cm^{-2} (a), and 20 mJ cm^{-2} (b). At a fluence of 5 mJ cm^{-2}, we used a T_L value of 843 K at 0 ps and 583 K at 1 ns in reference to Fig. 4a. At this fluence, the simulation replaced the extinction spectrum, for which at 0 ps has LSPR bleaching with both positive wings (black line in (a)), with one in which after 1 ns the positive wings are absent (red line in (a)). At a fluence of 20 mJ cm^{-2}, $T_L \geq 1336$ K was assumed. Three typical spectral shapes were reproduced in (b) depending on the medium temperature profile. The asymmetric bleaching spectral shape (blue line in (b)) occurs at the initial stage of excitation, when the medium temperature profile is very steep near the particle surface with a low refractive index of ~1.1. At a simulation time delay of 1 ns, a downward spectral shift of the right wing of the LSPR band results (red line in (b)). Here, because heat continues to conduct into the medium with time, the region of decreased refractive index expands.

Table 1. Refractive index (*n*), thermal conductivity (*k*), density (ρ) and heat capacity (C_p) of water in various states [1]

parameter	liquid water [2]	vapor bubble [3]	supercritical water [4]
n	1.33	1.0	1.2~1.1
k / W m^{-1} K^{-1}	0.61	0.0615	0.40
ρ / kg m^{-3}	1000	0.372	528
C_p / J kg^{-1} K^{-1}	4184	2014	5557

[1]   Ref. 43

[2]   293 K, 1 atm

[3]   573 K, 1 atm

[4]   873 K, 100 MPa

----

3. Particle evaporation in supercritical water.

At this pont, we present laser-fluence-dependent TEM images to show a clear picture of the pulsed-laser-induced events under a high pressure of 60 MPa. **Figure 7** shows the micrographs in conjunction with particle-size distribution histograms and extinction spectra. Fig. 7a shows the image without the picosecond-laser irradiation: spherical particles with diameter 59 ± 4 nm. When irradiated with laser fluence of 4.5 mJ cm^{-2} and 9.7 mJ cm^{-2}, practically no changes were observed after 70 shots (0.5 Hz) for the particle size and shape (see Fig. 7b for 4.5 mJ cm^{-2}). Additionally, the extinction spectral shape was barely affected. Note, however, when the colloid were irradiated with 1000 shots (0.5 Hz) at 9.7 mJ cm^{-2}, small fragments with < 10 nm were found coexisting with the particles of original size in TEM images. By contrast, when irradiated with a fluence of 19.6 mJ cm^{-2}, a number of small particles were produced along with 2–3 % of peculiar-shaped particles showing signs of eruption from the surface after 60 shots at 0.5 Hz. We give clear evidence of these erupted particles, with images of three examples (**Fig. 8**). We also note that, at a fluence of 19.6 mJ cm^{-2}, a small fraction of particles of 40–50 nm diameter appears in the histogram (Fig. 7c$_1$) correlated with a slight reduction in extinction peak intensity (Fig. 7c$_2$).

The observation of small particles with < 10 nm and AuNPs with a slightly reduced diameter (40–50 nm) in post-mortem TEM measurements is indicative of evaporation, forming size-reduced cores with small satellite particles formed from evaporated atoms and clusters. Previously, explosive evaporation was seen to take place, when colloidal AuNPs were heated to temperatures above the bp of gold by exposure to high-intensity nanosecond and picosecond laser illumination at ambient pressure.[44,45]. However, the potential generation of vapor bubbles did not materialize. Later, calculations[46] indicated that bubble formation around the NP makes the particle temperature uncontrollably high because of thermal shielding, resulting in polydispersed distribution of NP product size[44] (see also **ESI, S6**). To suppress the explosive evaporation, a technique was introduced to apply high pressures of 60–100 MPa during laser irradiation.[26,47] By applying high pressures exceeding the critical pressure, monodispersed AuNP products were obtained with average core

diameters strongly dependent on the laser fluence applied. High pressure was found to promote surface evaporation of AuNPs at temperatures between mp and bp of gold for the controlled reduction in core size.[27] Thus, applying high pressure proved to be a superb means to regulate particle temperature by tuning the heat dissipation to the surroundings while heating with lasers. The present TEM observation at 19.6 mJ cm^{-2} clearly demonstrated the absence of explosive evaporation by the direct observation of surface evaporation below the bp of gold.

In applying picosecond transient spectroscopy, the time scale for particle evaporation becomes of particular interest. However, in referring to Fig. 2, whether particle evaporation has occurred within 6 ns at 19.6 mJ cm^{-2} is unclear. According to a previous study,[27] evaporation may continue for time durations when particle temperatures are kept at mp $< T_L <$ bp. The condition is met at 19.6 mJ cm^{-2} because T_L of ~ 2000 K was estimated (Fig. 4c). The bp of gold is 3100 K under ambient pressure but at 60 MPa, it is estimated from the Clausius–Clapeyron equation to be 6200 K[48] and, hence, the particle is expected to be a liquid droplet. We believe that evaporation takes place more readily in the supercritical layer because of reduced density. Both small particles (Fig. 7c) and eruptions (Fig. 8) are signs of evaporation from liquid droplets because the droplets and evaporated species are both forced to cool down. The evaporated atoms and clusters tend to coalesce to form the small NPs that were observed by TEM measurement. The present study suggests that the dynamic expansion of the supercritical layer surrounding AuNP is prerequisite for the surface evaporation to occur.
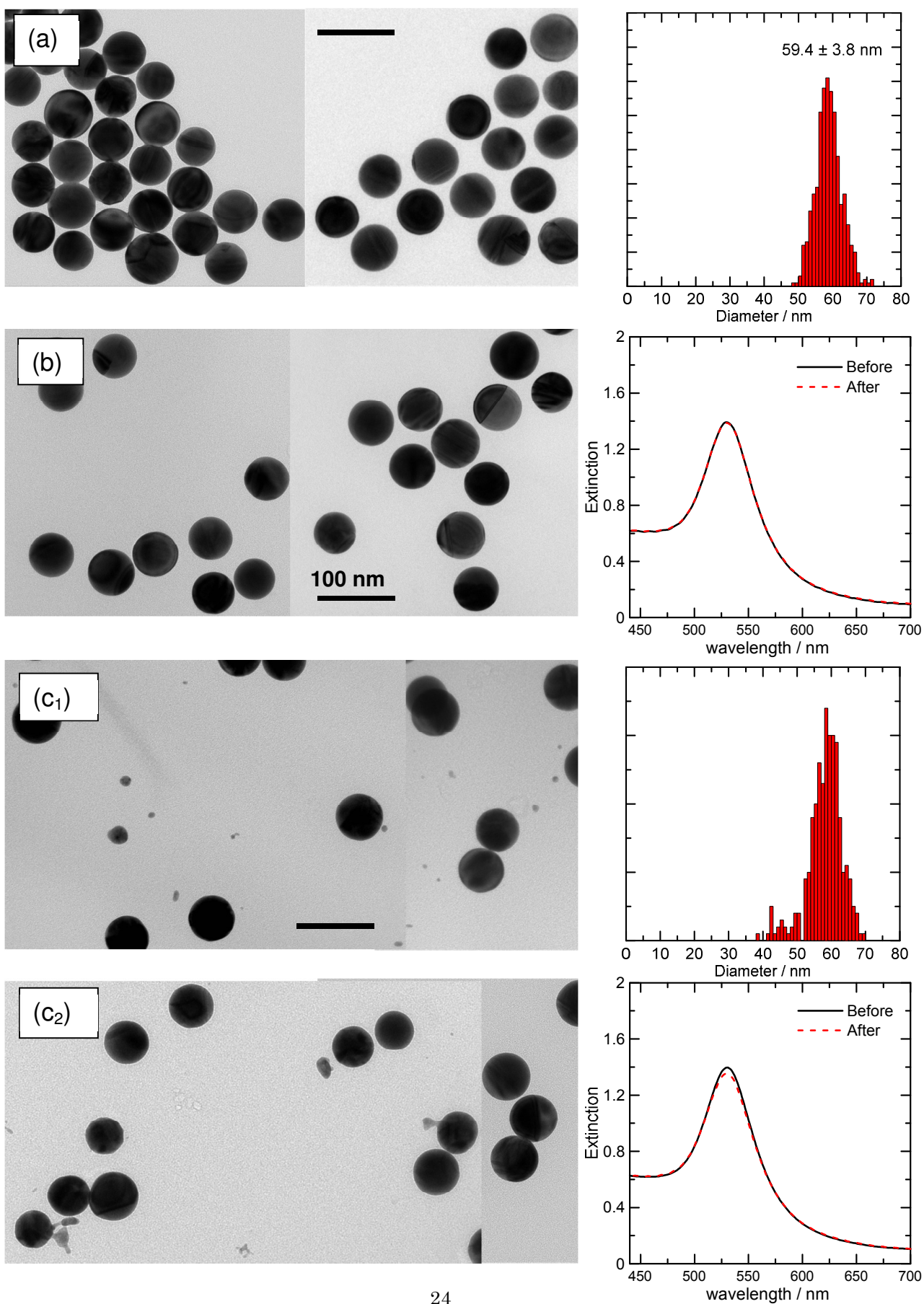

Fig. 7 TEM images, particle size distribution histograms, and extinction spectral changes for 15-ps pulsed laser irradiations at 355 nm under the external pressure of 60 MPa; (a) AuNPs with 59 ± 4 nm (obtained by Gaussian fitting) prior to the picosecond laser illumination, (b) after 70 shots of irradiation at 4.5 mJ cm^{-2}, and (c$_1$) and (c$_2$) after 60 shots of irradiation at 19.6 mJ cm^{-2}. In the histogram of (c$_1$), particles less than 10 nm in diameter were not shown in the histogram. The histogram in (c$_1$) shows the appearance of particles with slightly reduced diameters compared with the original particles. The scale bars represent 100 nm.
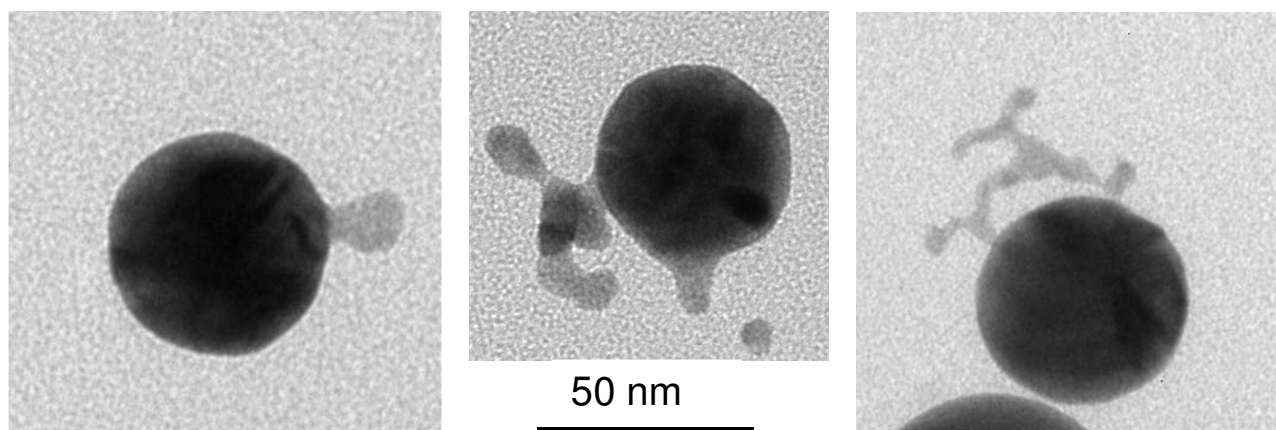
----

50 nm

Fig. 8 Magnified images of three erupted particles in Fig. 7c.

Conclusion

In this study, picosecond time-resolved extinction spectroscopy and temperature simulations revealed the formation of a surrounding supercritical water layer. The time evolution and dissipation of supercritical water layer have been characterized spectroscopically for the first time. The two observations, evaporation below bp and supercritical layer formation, have important implications to the mechanistic aspect of laser AuNP interaction, leading to a phase change in both particle and local medium. This study has demonstrated the critical role of the phase change in the medium to the laser-induced evaporation of AuNPs. Further characterization of the dynamic nature of the supercritical layer is of importance to promote better understanding of this unique species because of the seemingly big difference from its static counterpart formed under steady-state heating. The study of transient Raman spectroscopy, which is more helpful than our transient extinction spectroscopy to pursue both expansion and collapse of supercritical layer, is ongoing.

References

1. A. O. Govorov and H. H. Richardson, *Nano Today*, 2007, **2**, 30–38.

2. Z. Qin and J. C. Bischof, *Chem. Soc. Rev.* 2012, **41**, 119–1217.

3. D. Boyer, P. Tamarat, A. Maali, B. Lounis and M. Orrit, *Science*, 2002, **297**, 1160–1163.

4. A. Gaiduk, P. V. Ruijgrok, M. Yorulmaz and M. Orrit, *Chem. Sci.*, 2010, **1**, 343–350.

5. D. Lapotko, Cancer, 2011, **3**, 802–840.

6. E. Y. Lukianova-Hleb, X. Ren, R. R. Sawant, X. Wu, V. P. Torchilin and D. O. Lapotko, *Nature Medicine*, 2014, **20**, 778–784.

7. U. Kreibig and M. Vollmer, *Optical Properties of Metal Clusters*; Springer: Berlin, 1995.

8. J. N. Anker, W. P. Hall, O. Lyanders, N. C. Shah, J. Zhao and R. P. Van Duyne, *Nature Mat*. 2008, **7**, 442–453.

9. K. M. Mayer and J. H. Hafner, *Chem. Rev*. 2011, **111**, 3828–3857.

10. P. Wang, B. Huang, Y. Dai, and M-H. Whangbo, *Phys. Chem. Chem. Phys.* 2012, **14**, 9813–9825.

11. X. Zhang, Y. L. Chen, R-S. Liu and D. P. Tsai, *Rep. Prog. Phys*. 2013, **76**, 046401.

12. H. A. Atwater and A. Polman, *Nature Mat*. 2010, **9**, 205–213.

13. S. Link and M. A. El-Sayed, *Int. Rev. Phys. Chem*. 2000, **19**, 409–453.

14. C. Burda, X. Chen, R. Narayanan and M. A. El-Sayed, *Chem. Rev.*, 2005, **105**, 1025–1102.

15. G. V. Hartland, *Chem. Rev*. 2011, **111**, 3858–3887.

16. G. V. Hartland, *Ann. Rev. Phys. Chem*. 2006, **57**, 403–430.

17. A. Tchebotareva, P. V. Ruijgrok, P. Zijlstra and M. Orrit, Laser. *Photon. Rev*. 2010, **4**, 581–597.

18. S. Link and M. A. El-Sayed, *J. Phys. Chem. B* 1999, **103**, 8410–8426.

19. S. Hashimoto, D. Werner and T. Uwada, *J. Photochem. Photobiol. C: Rev*. 2012, **13**, 28–54.

20. V. Kotaidis, C. Dahmen, G. Von Plessen, F. Springer, A. Plech, *J. Chem. Phys.* 2006, **124**,

184702.

21. D. Lapotko, *Opt. Express* 2009, **17**, 2538–2556.

22. T. Katayama, K. Setoura, D. Werner, H. Miyasaka and S. Hashimoto, *Langmuir*, 2014, **30**, 9504–9513.

23. H. Weingärtner and E. U. Franck, *Angew. Chem. Int. Ed.* 2005, **44**, 2672–2692.

24. E. Boulais, R. Lachanine and M. Meunier *Nano. Lett*. 2012, **12**, 4763–4769.

25. G. Frens, *Nature Phys. Sci.*, 1973, **241**, 20–22.

26. D. Werner and S. Hashimoto, *Langmuir* 2013, **29**, 1295–1302.

27. M. Strasser, K. Setoura, U. Langbein, and S. Hashimoto, *J. Phys. Chem. C* 2014, **118**, 25748– 25755.

28. W. Yang, *Appl. Opt.* 2003, **42**, 1710–1720.

29. M. Kerker, The Scattering of Light and other Electromagnetic Radiation. Academic Press, New York, 1969.

30. J.-P. Schäfer, Implementierung und Anwendung analytischer und numerischer Verfahren zur Lösung der Maxwellgleichungen für die Untersuchung der Lichtausbreitung in biologischem Gewebe, PhD thesis, Ulm University, 2011.

31. P. Grua and H. Bercegol, *Proc. SPIE* 2000, **4347**, 579–587.

32. M. Otter, *Z. Phys*. 1961, **161**, 539–549.

33. H. Inouye, K. Tanaka, I. Tanahashi and K. Hirao, *Phys. Rev. B* 1998, **57**, 11334–11340.

34. M. Hu and G. V. Hartland, *J. Phys. Chem. B*, 2002, **106**, 7029–7033.

35. R. Fedosejevs, R. Ottmann, R. Sigel, G. Kuehnle, S. Szatmari and F. P. Schaefer, *Phys. Rev. Lett.* 1990, **64**, 1250–1253.

36. P. Gibbon and P. E. Foerster, *Plasma Phys. Control Fusion* 1996, **38**, 769–793.

37. Z. Ge, D. G. Cahill and P. V. Braun, *J. Phys. Chem. B*, 2004, **108**, 18870–18875.

38. A. Plech, V. Kotaidis, S. Gresillon, D. Dahmen, G. von Plessen, *Phys. Rev. B* 2004, **70**, 195423.

39. T. Stoll, P. Maioli, A. Crut, S. Rodal-Cedeira, I. Pastoriza-Santos, F. Vallee, N. Del Fatti, *J. Phys.*

Chem. C 2012, **116**, 5482–5491.

40. D. Werner, A. Furube, T. Okamoto and S. Hashimoto, *J. Phys. Chem. C* 2011, **115**, 8503–8512.

41. C. F. Bohren and D. R. Huffman, *Absorption and Scattering of Light by Small Particles*; Wiley: New York, 1983.

42. K. Setoura, D. Werner and S. Hashimoto, *J. Phys. Chem. C*, 2012, **116**, 15458–15466.

43. L. Haar, J. S. Gallagher and G. S. Kell, NBS/NRC Steam Tables, Hemisphere Publishing: Washington DC, 1976.

44. A. Takami, H. Kurita and S. Koda, *J. Phys. Chem. B* 1999, **103**, 1226–1232.

45. D. Werner, S. Hashimoto and T. Uwada, *Langmuir* 2010, **26**, 9956–9963.

46. D. Werner and S. Hashimoto, *J. Phys. Chem. C*, 2011, **115**, 5063–5072.

47. D. Werner, T. Ueki and S. Hashimoto, *J. Phys. Chem. C* 2012, **116**, 5482–5491.

48. P. W. Atkins and J. de Paula, *Physical Chemistry*; 10th ed., Oxford University Press: Oxford, 2014, p. 169.